

Deformation of a vortex ring caused by its impingement on a sphere

Cite as: Phys. Fluids **31**, 107108 (2019); <https://doi.org/10.1063/1.5122260>

Submitted: 30 July 2019 . Accepted: 12 October 2019 . Published Online: 28 October 2019

Van Luc Nguyen , Kotaro Takamure (高牟礼 光太郎) , and Tomomi Uchiyama (内山 知実) 

COLLECTIONS

 This paper was selected as an Editor's Pick



View Online



Export Citation



CrossMark

ARTICLES YOU MAY BE INTERESTED IN

[Jeffery orbits in shear-thinning fluids](#)

Phys. Fluids **31**, 103106 (2019); <https://doi.org/10.1063/1.5125468>

[Hydrodynamics of a rigid stationary flat plate in cross-flow near the free surface](#)

Phys. Fluids **31**, 102108 (2019); <https://doi.org/10.1063/1.5111525>

[Modification of three-dimensional instability in the planar shear flow around two circular cylinders in tandem](#)

Phys. Fluids **31**, 104110 (2019); <https://doi.org/10.1063/1.5120564>



NEW: TOPIC ALERTS

Explore the latest discoveries in your field of research

[SIGN UP TODAY!](#)

Deformation of a vortex ring caused by its impingement on a sphere

Cite as: *Phys. Fluids* **31**, 107108 (2019); doi: [10.1063/1.5122260](https://doi.org/10.1063/1.5122260)

Submitted: 30 July 2019 • Accepted: 12 October 2019 •

Published Online: 28 October 2019






View Online



Export Citation



CrossMark

Van Luc Nguyen,^{1,a)}  Kotaro Takamure (高牟礼 光太郎),²  and Tomomi Uchiyama (内山 知実)² 

AFFILIATIONS

¹Graduate School of Informatics, Nagoya University, Nagoya, Japan

²Institute of Materials and Systems for Sustainability, Nagoya University, Nagoya, Japan

^{a)} Author to whom correspondence should be addressed: nguyen.luc.van@j.mbox.nagoya-u.ac.jp

ABSTRACT

The deformation of a vortex ring caused by its impingement on a sphere was numerically investigated using a proposed vortex-in-cell method. The method was validated by simulation of the collision of a vortex ring with a rigid planar surface and proved to be most satisfactory in the analysis of the dynamics of a vortex structure. In a coaxial collision, the behavior of the vortex structure is similar to that in the case of a planar surface. A secondary vortex ring is formed owing to the separation of the boundary layers on the sphere, caused by the effect of the primary vortex ring. The interaction between the secondary and primary vortex rings plays an important role in the dynamics of the vortex structure when the secondary vortex ring is completely formed. In a noncoaxial collision, the structure of the secondary vortex is moderately different from that in the coaxial collision. Moreover, the vortex structure in the coaxial collision is two-dimensional, in which the vorticity field is dominated by two transverse components, whereas that in the noncoaxial collision is three-dimensional. The total kinetic energy in both the cases decreases gradually during the entire period of evolution, whereas the enstrophy reduces in the early stage, then increases considerably, before a gradual reduction in the final stage. The enstrophy reaches a peak when the secondary vortex ring is completely formed, at which stage the effects of vortex stretching and vorticity production at the solid boundary are higher than that of vortex diffusion.

Published under license by AIP Publishing. <https://doi.org/10.1063/1.5122260>

I. INTRODUCTION

Vortex dynamics is the key to understanding the phenomena in fluid dynamics that are observed in both environmental processes and engineering applications such as leapfrogging of circular vortex rings,¹ evolution of an elliptic vortex ring,² airplanes,³ bridge piers, and heat exchangers.⁴ A comprehensive understanding of the flow phenomena is important for improving design- and control-related engineering devices. Many researchers have made considerable efforts in extending their knowledge of the phenomena in vortex dynamics. Among these, the impingement of a vortex ring on a rigid surface has been used widely to study the dynamics of the vortex structure. The employed rigid surfaces are a planar surface,^{5–11} an inclined planar surface,^{12,13} a rough surface,¹⁴ a permeable surface,¹⁵ a cylindrical surface,¹⁶ and a spherical surface.^{17,18} Allen *et al.*¹⁷ investigated the symmetric collision of a vortex ring with a moving sphere, in which the diameter of the vortex ring

is larger than that of the sphere. The primary vortex ring passes through the sphere followed by the secondary vortex ring. The collision of a vortex ring with a sphere of a larger diameter, such that the vortex ring does not pass through the sphere, was not investigated. Felderhofa¹⁸ proposed a theory of the collision of a vortex ring with a sphere to predict the behavior of the flow. However, this theory is limited in the case of an inviscid incompressible flow, i.e., the vortex diffusion (the viscous term in the Navier–Stokes equations) effects are neglected. In this study, the deformation of a vortex ring caused by its impingement on a larger sphere in a viscous incompressible fluid was numerically investigated using a vortex-in-cell (VIC) method and the characteristics of vortex dynamics were explained.

The VIC method is a hybrid Eulerian–Lagrangian vortex method, also known as a remeshed vortex particle method. It uses the vortex particles transporting the flow quantities in a Lagrangian frame with grid-based formulas to calculate the flow fields. In this

method, the fluid flow is discretized into vortex particles that carry the flow momentum in terms of vorticity and move at the flow velocity given at the location of the particles. After moving to the Lagrangian locations, the vortex particles are redistributed onto the Eulerian grid while ensuring that the flow momentum is conserved. Subsequently, the velocities and vorticities of the vortex particles are calculated by solving the Poisson and momentum equations on the grid, respectively. Compared to the traditional Eulerian methods, the VIC method has the advantages of the Lagrangian vortex methods in the analysis of vortex dynamics such as formation, deformation, breakdown, coalescence, and decay of eddies of various scales. It also offers a lower numerical dissipation or diffusion when solving the convection term in a linear form.¹⁹ Moreover, in solving the linear convection term and redistribution of the vortex particles, the Courant–Friedrichs–Lewy condition to guarantee the simulation convergence is not required, leading to a choice of a larger time step that can adapt to the simulation. Compared to the Lagrangian vortex methods, this method avoids a high cost in the calculation of the velocity of the vortex elements obtained using the Biot–Savart integral with $\mathcal{O}(N^2)$ operations, where N is the number of vortex elements. The cost can be reduced significantly when the Poisson equation is solved on the grid using the iterative successive overrelaxation (SOR) method with $\mathcal{O}(N^{3/2})$ operations or the direct fast Fourier transform (FFT) method with $\mathcal{O}(N \log_2 N)$ operations, where N is the number of grid nodes. In addition, this method overcomes the problem of distortion in the vortex distribution that occurs in the Lagrangian vortex methods. Owing to the nature of the features of the Lagrangian description and fluid strain, there is a clustering of vortex elements leading to their deficiency in some regions, where a certain number of vortex elements is required to maintain the continuity of the vorticity field.²⁰ The redistribution of vortex particles onto the Eulerian grid in the calculation procedure resolves this problem adequately. Moreover, the use of grid-based formulas allows a combination of the VIC method and an immersed boundary method to enforce the no-slip condition of flow on moving bodies having complex geometries. This has the advantage of a smart grid in which the flow quantities can be discretized in a consistent manner to improve the accuracy of the method.²¹ Therefore, the VIC method has the advantages of the Eulerian mesh-based methods as well as the Lagrangian mesh-free methods and limits the disadvantages of each.

The VIC method was introduced to simulate inviscid incompressible flows by Christiansen²² and adapted later for viscous incompressible flows by Cottet and Koumoutsakos.²³ The method was combined with the penalization method (a type of immersed boundary method) to simulate the flow around a moving body by Cottet and Poncet.¹⁹ The accuracy of the method was improved using staggered-grid schemes in the investigation by Uchiyama *et al.*²¹ Subsequently, the VIC method was proved to be robust and efficient to simulate flows around two tandem cylinders.²⁴ Moreover, it was also suitable to be applied to simulations of gas–liquid two-phase flows.^{25–28} In this study, based on previous investigations,^{21,24} a VIC method was developed to simulate the deformation of a vortex structure caused by its impingement on a rigid body surface. The remainder of this paper is organized as follows: the numerical method is detailed in Sec. II, the results are discussed in Sec. III, and the conclusions are presented in Sec. IV.

II. NUMERICAL METHODS

A. Basic equations

The mass and momentum Navier–Stokes equations for the flow of a viscous incompressible fluid in a domain Ω are written in convective form as

$$\nabla \cdot \mathbf{u} = 0, \quad \mathbf{x} \in \Omega, \quad (1)$$

$$\frac{\partial \mathbf{u}}{\partial t} + (\mathbf{u} \cdot \nabla) \mathbf{u} = -\frac{1}{\rho} \nabla p + \nu \nabla^2 \mathbf{u} + \mathbf{g}, \quad (2)$$

where $\mathbf{x} = (x, y, z)$, $\mathbf{u} = (u, v, w)$, p , ν , t , and \mathbf{g} are the coordinate, velocity, pressure, kinematic viscosity, time, and gravitational acceleration, respectively. Taking the curl operation on both sides of Eq. (2), the momentum equation for the fluid flow is written in vorticity–velocity form as

$$\frac{\partial \boldsymbol{\omega}}{\partial t} + (\mathbf{u} \cdot \nabla) \boldsymbol{\omega} = (\boldsymbol{\omega} \cdot \nabla) \mathbf{u} + \nu \nabla^2 \boldsymbol{\omega}, \quad (3)$$

where the vorticity field is defined as

$$\boldsymbol{\omega} = \nabla \times \mathbf{u}. \quad (4)$$

In Eq. (3), the second term on the left is vortex convection, and the first and second terms on the right are vortex stretching and diffusion, respectively. The vortex convection $(\mathbf{u} \cdot \nabla) \boldsymbol{\omega}$ expresses the motion of vortices with the conservation of the flow momenta and their shapes. The vortex stretching $(\boldsymbol{\omega} \cdot \nabla) \mathbf{u}$ represents the lengthening of vortices in the three-dimensional fluid flow, associated with a corresponding increase of the component of vorticity in the stretching direction. In other words, the vortex stretching expresses the interaction between the local vector vorticity $\boldsymbol{\omega}$ and the velocity gradient $\nabla \mathbf{u}$. In turbulent flows, the vortex stretching is the cause of the process of the turbulence energy cascade involving the transfer of energy from the large scales of motion to the small scales. The vortex diffusion $\nu \nabla^2 \boldsymbol{\omega}$ accounts for the diffusion of vortices by viscosity. The vector velocity, based on Helmholtz’s theorem, is decomposed into an irrotational vector field $\nabla \phi$ and a solenoidal vector field $\nabla \times \boldsymbol{\psi}$ as

$$\mathbf{u} = \nabla \phi + \nabla \times \boldsymbol{\psi}, \quad (5)$$

where $\boldsymbol{\psi}$ and ϕ are the vector and scalar potentials of the velocity field, respectively. Taking the curl of Eq. (5) and substituting the properties of the irrotational and solenoidal vector fields, $\nabla \times (\nabla \phi) = 0$ and $\nabla \cdot \boldsymbol{\psi} = 0$, respectively, into the result, the Poisson equation for $\boldsymbol{\psi}$ is derived as

$$\nabla^2 \boldsymbol{\psi} = -\boldsymbol{\omega}. \quad (6)$$

The Laplace equation for ϕ is obtained by substituting Eq. (5) into Eq. (1) as

$$\nabla^2 \phi = 0. \quad (7)$$

B. Vortex-in-cell method

In the VIC method, the fluid is discretized into vortex particles p at location \mathbf{x}_p , moving at a speed of $\mathbf{u}(\mathbf{x}_p)$ given by the flow velocity at the particle location, and carrying the vorticity $\boldsymbol{\omega}(\mathbf{x}_p)$. The momentum equation for the fluid flow, Eq. (3), is rewritten in the Lagrangian form of vortex particles as

$$\frac{d\mathbf{x}_p}{dt} = \mathbf{u}(\mathbf{x}_p), \quad (8)$$

$$\frac{d\boldsymbol{\omega}(\mathbf{x}_p)}{dt} = (\boldsymbol{\omega}(\mathbf{x}_p) \cdot \nabla)\mathbf{u}(\mathbf{x}_p) + \nu \nabla^2 \boldsymbol{\omega}(\mathbf{x}_p). \quad (9)$$

Initially, the vortex particles are located on the grid and their vorticities $\boldsymbol{\omega}(\mathbf{x}_p)$ are calculated using Eq. (9) to account for the vortex diffusion and stretching. Subsequently, they convect, according to Eq. (8), carrying their updated vorticities $\boldsymbol{\omega}(\mathbf{x}_p)$. The particle velocity $\mathbf{u}(\mathbf{x}_p)$ is computed using Eq. (5), in which ψ and ϕ are obtained by solving the Poisson and Laplace equations (6) and (7) on the grid, respectively. After the particle convection, the vortex particles with vorticities $\boldsymbol{\omega}(\mathbf{x}_p)$ at the Lagrangian points \mathbf{x}_p are redistributed onto the grid nodes \mathbf{x}_q while ensuring the conservation of the flow momentum. The vorticity of the vortex particles on the grid nodes, $\boldsymbol{\omega}(\mathbf{x}_q)$, is attained by interpolating from that of vortex particles on the Lagrangian points, $\boldsymbol{\omega}(\mathbf{x}_p)$, as

$$\boldsymbol{\omega}(\mathbf{x}_q) = \sum_p^{N_p} \boldsymbol{\omega}(\mathbf{x}_p) W\left(\frac{x_q - x_p}{\Delta x}\right) W\left(\frac{y_q - y_p}{\Delta y}\right) W\left(\frac{z_q - z_p}{\Delta z}\right), \quad (10)$$

where $\mathbf{x}_q = (x_q, y_q, z_q)$, $\mathbf{x}_p = (x_p, y_p, z_p)$, Δx , Δy , and Δz are the cell widths, N_p is the number of vortex particles, and $W(x)$ is a third-order accurate kernel-interpolation function,²³

$$W(x) = \begin{cases} 1 - \frac{5}{2}|x|^2 + \frac{3}{2}|x|^3 & \text{if } |x| \leq 1, \\ \frac{1}{2}(2 - |x|)^2(1 - |x|) & \text{if } 1 < |x| \leq 2, \\ 0 & \text{if } |x| > 2. \end{cases} \quad (11)$$

The vorticity is a solenoidal vector field, i.e., $\nabla \cdot \boldsymbol{\omega} = 0$. However, when solving the momentum equation (9) and redistributing the particles from the Lagrangian to Eulerian locations (10) the vorticity does not satisfy the above-mentioned property, i.e., $\nabla \cdot \boldsymbol{\omega} \neq 0$ and must be corrected in the simulation procedure. There are two approaches used widely to correct the vorticity field such as the projection method explained in detail in Ref. 28 and a method in which the vorticity field is modified using Eq. (4)²¹ because of

$$\nabla \cdot \boldsymbol{\omega} = \nabla \cdot (\nabla \times \mathbf{u}) = \nabla \times (\nabla \cdot \mathbf{u}) = 0. \quad (12)$$

In the current study, the vorticity is corrected using Eq. (4) after every 50 time steps.

C. Penalization method

The penalization method was combined with the VIC method to implement the no-slip condition of fluid flow on the solid body surface.¹⁹ In the penalization method, the momentum equation of fluid flow, Eq. (3), is rewritten as follows:

$$\frac{\partial \boldsymbol{\omega}}{\partial t} + (\mathbf{u} \cdot \nabla)\boldsymbol{\omega} = (\boldsymbol{\omega} \cdot \nabla)\mathbf{u} + \nu \nabla^2 \boldsymbol{\omega} + \nabla \times (\lambda \chi_s (\mathbf{u}_s - \mathbf{u})), \quad (13)$$

where λ is the penalization parameter, \mathbf{u}_s is the solid body velocity, and χ_s identifies the solid and fluid regions. \mathbf{u}_s and χ_s are calculated as

$$\mathbf{u}_s = \mathbf{u}_s^1 \cup \mathbf{u}_s^2 \cup \dots \cup \mathbf{u}_s^{N_b}, \quad \mathbf{x} \in \Omega, \quad (14)$$

$$\chi_s = \chi_s^1 \cup \chi_s^2 \cup \dots \cup \chi_s^{N_b}, \quad \mathbf{x} \in \Omega, \quad (15)$$

respectively, where the superscripts 1, 2, and N_b indicate the first, second, and N_b th bodies immersed in the fluid, respectively. Each χ_s^i , $i = 1, 2, \dots, N_b$, is expressed as

$$\chi_s^i(\mathbf{x}) = \begin{cases} 1 & \text{if } \mathbf{x} \in S_i, \\ 0 & \text{if } \mathbf{x} \in \Omega \setminus S_i, \end{cases} \quad (16)$$

where S_i denotes the solid region occupied by the i th body. In the penalization method, the fluid is treated as a continuous phase throughout the solid body by smoothing the value of χ_s^i near the fluid–solid interface using the following Heaviside function:

$$\chi_s(d^i) = \begin{cases} 0 & \text{if } d^i < -\varepsilon, \\ \frac{1}{2} \left[1 + \frac{d^i}{\varepsilon} + \frac{1}{\pi} \sin\left(\pi \frac{d^i}{\varepsilon}\right) \right] & \text{if } |d^i| \leq \varepsilon, \\ 1 & \text{if } d^i > \varepsilon, \end{cases} \quad (17)$$

where d^i is the sign distance from the grid node to the surface of the i th solid body shown in Fig. 1 and ε is set to be $\sqrt{3}\Delta x$. If the two solid bodies touch each other, χ_s^i is calculated as

$$\chi_s^i(\mathbf{x}) = \max(\chi_s^i(\mathbf{x}), \chi_s^j(\mathbf{x})), \quad \mathbf{x} \in S^i \cap S^j. \quad (18)$$

The no-slip condition of the flow is enforced over a region with a thickness of 2ε along the body surface. The nonzero values of the velocity and vorticity fields still exist inside near the solid body. The values of the flow quantities such as vorticity fluxes and shear stresses on the solid body surface are not captured accurately. However, the method can reproduce well the flow characteristics around the solid body. Applying the splitting method to Eq. (13), the penalization velocity is expressed as

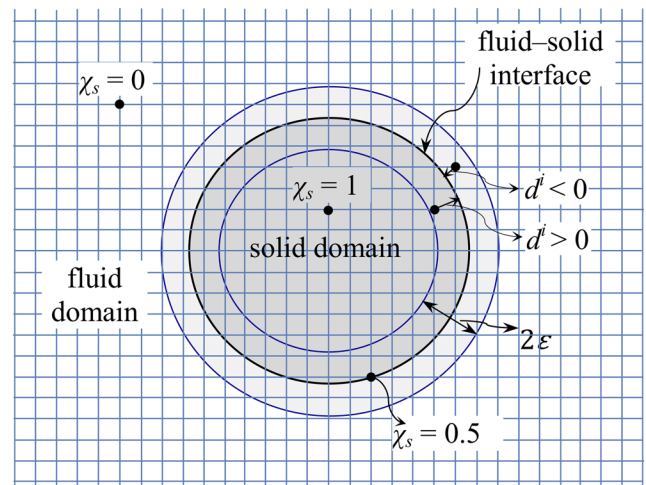


FIG. 1. Two-dimensional configuration of the fluid region and solid region occupied by the i th body. d^i indicates the sign distance from the grid node to the body surface. 2ε is the thickness of the region along the solid surface in which the flow penetrates. χ_s identifies the fluid and solid regions, and its value equals 0, 1, and 0.5 when the grid nodes are in the fluid, solid regions, and on the solid body surface, respectively. χ_s is smoothed using the Heaviside function when the grid node near the body surface.

$$\frac{\partial \mathbf{u}}{\partial t} = \lambda \chi_s (\mathbf{u}_s - \mathbf{u}). \quad (19)$$

By choosing $\lambda = 1/\Delta t$, where Δt is the time step, and applying the forward finite-difference scheme, the penalization velocity is derived as

$$\mathbf{u}_\lambda = (1 - \chi_s) \mathbf{u} + \chi_s \mathbf{u}_s. \quad (20)$$

The penalization vorticity is calculated by a summation of its previous simulation-time-step value, and the change in it is obtained from the change in velocity and is derived as

$$\boldsymbol{\omega}_\lambda = \boldsymbol{\omega} + \nabla \times (\mathbf{u}_\lambda - \mathbf{u}). \quad (21)$$

D. Numerical procedure

If the flow quantities at time t are known, the flow at time $(t + \Delta t)$ is calculated by the following procedure:

- calculate the vorticity of the vortex particle $\boldsymbol{\omega}(x_p)$ using Eq. (9) to account for the vortex stretching and diffusion,
- calculate the convection of the vortex-particle x_p using Eq. (8),
- redistribute the vortex particle from the Lagrangian to Eulerian points using Eq. (10),
- calculate the vector potential of the velocity $\boldsymbol{\psi}$ using Eq. (6),
- calculate the scalar potential of the velocity ϕ using Eq. (7),
- calculate the fluid velocity \mathbf{u} using Eq. (5),
- correct the vorticity field $\boldsymbol{\omega}_{corrected}$ to satisfy the solenoidal condition using Eq. (4),
- calculate the solid velocity \mathbf{u}_s using Eq. (14),
- calculate χ_s using Eq. (15) to identify the solid and fluid regions,
- calculate the penalization velocity \mathbf{u}_λ using Eq. (20) to enforce the no-slip condition of flow on the body surface,
- calculate the penalization vorticity $\boldsymbol{\omega}_\lambda$ using Eq. (21), and
- initialize the values of the velocity and vorticity fields $\mathbf{u} = \mathbf{u}_\lambda$ and $\boldsymbol{\omega} = \boldsymbol{\omega}_\lambda$, respectively, for the next time step.

In this study, the fourth-order accurate staggered-grid finite-difference schemes are applied to spatial derivatives. The convection of the particle, Eq. (8), is solved using the first-order accurate forward-finite-difference scheme and the temporal variation of Eq. (9) is solved using the second-order Adams–Bashforth method. The simulation is tested using the convective outflow condition detailed in Ref. 28 as well as the periodic condition, in which the Poisson equation (6), is solved by using the SOR method or FFT method. The same simulation results are obtained using both the conditions. The computational cost of solving the Poisson equation using the FFT method is much lower than that using the SOR method. Therefore, the periodic condition is applied to simulations.

III. RESULTS AND DISCUSSION

A. Collision of a vortex ring with a plane

A simulation of the collision of a vortex ring with a solid plane is implemented to evaluate the ability of the method to examine the deformation of a vortex caused by its impingement on a solid body surface. The conditions of the simulation are the same as those in an

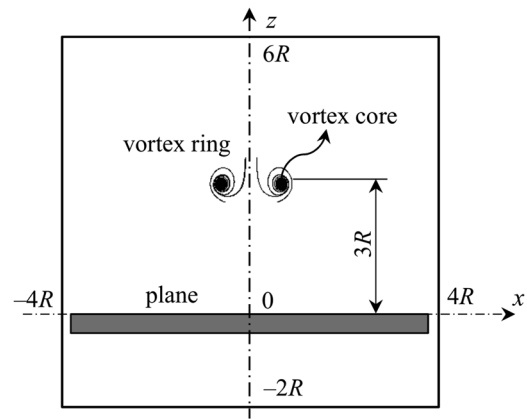


FIG. 2. Two-dimensional configuration of initial conditions of collision of a vortex ring with a solid plane: The computational domain is $(-4R, 4R) \times (-4R, 4R) \times (-2R, 6R)$. The vortex ring is described by a Gaussian distribution function. The vortex ring has radius R , a core radius $\sigma = 0.21R$, a circulation $\Gamma_0 = 1$, at the initial position of $(x_0, y_0, z_0) = (0, 0, 3R)$, at $Re_\Gamma = 1743$, and the distance between the vortex ring and the plane is $3R$.

experimental investigation by Chu *et al.*⁹ The configuration of the initial conditions of the simulation is shown in Fig. 2. A vortex ring at the outset of the simulation is described by a Gaussian distribution function as

$$\omega_\theta = \frac{\Gamma_0}{\pi \sigma^2} e^{-\frac{\rho^2(x,y,z)}{\sigma^2}}, \quad (22)$$

where

$$\rho^2(x, y, z) = (R - \sqrt{(x - x_0)^2 + (y - y_0)^2})^2 + (z - z_0)^2. \quad (23)$$

The vortex ring has a radius R , a core radius $\sigma = 0.21R$, and an initial circulation $\Gamma_0 = 1$, moving vertically downward at a Reynolds number ($Re_\Gamma = \Gamma_0/\nu$) of 1743, at the initial position of $(x_0, y_0, z_0) = (0, 0, 3R)$. The initial distance between the vortex ring and plane is $3R$. A computational domain of $(-4R, 4R) \times (-4R, 4R) \times (-2R, 6R)$ is divided into four grid resolutions of cube cells as discussed later and the nondimensional time step, $\Delta t^* = \Delta t \Gamma_0 / R^2$, is 0.005. The nondimensional flow quantities are defined as $t^* = t \Gamma_0 / R^2$, $w^* = wR / \Gamma_0$, $\omega_y^* = \omega_y R^2 / \Gamma_0$, and $|\boldsymbol{\omega}^*| = |\boldsymbol{\omega}| R^2 \Gamma_0$.

Figure 3 shows the effect of grid resolution on the results of simulation. The profiles of the velocity and vorticity at the lowest grid resolution of $120 \times 120 \times 120$ nodes are quite different from those at other grid resolutions. With an increase in grid resolution, these profiles approach those at the highest grid resolution of $240 \times 240 \times 240$ nodes. Therefore, the results of simulation are convergent with an increase in the grid resolution. The relative errors in these profiles at two grid resolutions, namely, $200 \times 200 \times 200$ nodes and $240 \times 240 \times 240$ nodes, are calculated as

$$\frac{|\max(w_{(200 \times 200 \times 200)}^*) - \max(w_{(240 \times 240 \times 240)}^*)|}{\max(w_{(240 \times 240 \times 240)}^*)} = 6\%, \quad (24)$$

$$\frac{|\max(\omega_{y(200 \times 200 \times 200)}^*) - \max(\omega_{y(240 \times 240 \times 240)}^*)|}{\max(\omega_{y(240 \times 240 \times 240)}^*)} = 0.04\%. \quad (25)$$

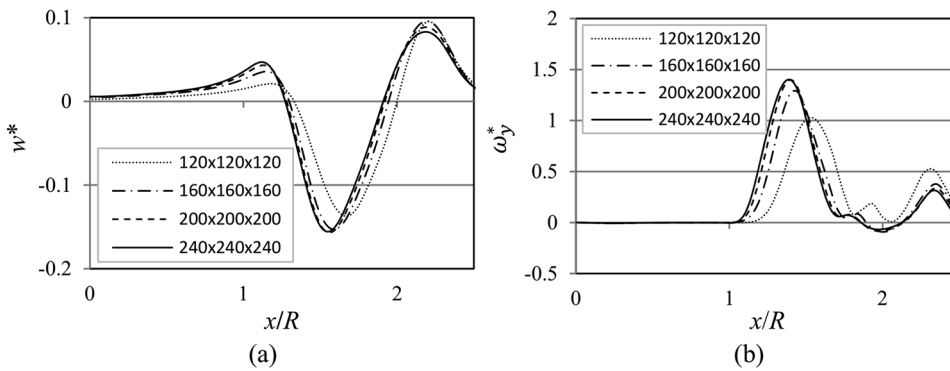


FIG. 3. Convergence study: Profiles of vertical velocity w^* and vorticity component ω_y^* along a horizontal line passing through the vortex ring center at $t^* = 24$ at four grid resolutions, as shown in the legend.

These errors are acceptable and the grid resolution of $200 \times 200 \times 200$ nodes is applied to the other simulations. Moreover, a simulation with a computation domain of $(-5R, 5R) \times (-5R, 5R) \times (-2R, 6R)$ and a grid resolution of $250 \times 250 \times 200$ nodes is tested and shows that the computational domain does not affect the results. In this study, the investigation of the effects of the time step upon the simulation results are not carried out. However, the time step used in this simulation is referenced from the simulation of the collision of a vortex ring with a circular cylinder²⁸ and it was proved to be good enough to capture the dynamics of the collision of a vortex with a solid surface.

Figure 4 describes the time evolution of distribution of the vorticity component ω_y on the x - z plane passing through the centerline of the vortex ring. As the vortex ring moves toward the plane, the boundary layers are formed on the plane, as shown at $t^* = 6$ in the middle column of the figure. This is due to the effect of the ambient flow of the vortex ring, induced as a consequence of the spread of the vorticity. At $t^* = 12$, the layers appear to be compressed by the primary vortex ring, leading to their separation from the plane. Subsequently, they roll up to form the secondary vortex ring at $t^* = 16$ and interact with the primary ring at $t^* = 18$. From $t^* = 20$, the secondary vortex ring moves around the primary ring and the boundary layers continue to separate from the plane owing to the effect of the primary vortex ring. There are some differences between the results obtained by the simulation and the experiment due to improper visualization of the vortex structure by the experiment. In the experiment, the ink is used to represent the movement of fluid particles. The ink injected only from the cylinder is transported by the flow moving from the inside to the outside of the cylinder. The movement of fluid particles carrying the ink forms the primary vortex ring which is observed completely. However, there is no ink injected from the sphere surface; therefore, the movement of fluid particles around the sphere is not represented. The formation of the boundary layers and the secondary vortex ring, as shown at $t^* = 6, 12$, and 16 in the left column of the figure, is not satisfactory. The ink visualizing the primary vortex ring is extracted by the secondary ring and the boundary layers to form thin layers, as shown at $t^* = 16, 18$, and 20 . The interactions between the primary and secondary vortex rings as well as the primary vortex ring and the boundary layers are observed. In general, the time evolution of the vortex structure observed by the present simulation (VIC) agrees with that obtained by the experiment (Expt.)⁹ and the Lattice Boltzmann method (LBM).¹⁵ This proves that the present numerical method can capture the

characteristics of the dynamics of a vortex ring impinging on a rigid solid body.

Figure 5 shows a comparison of the displacement of the primary vortex core on the x - z plane as obtained by the Expt., the finite different method (FDM),⁹ the LBM,¹⁵ and the VIC. The vorticity at the center of the vortex ring is negligible, whereas that at the center of the vortex core is almost maximum. In the present investigation, the displacement of the primary vortex core is estimated as

$$x_c = \frac{\iint_H x \omega_y^*}{\iint_H \omega_y^*}, \quad (26)$$

$$z_c = \frac{\iint_H z \omega_y^*}{\iint_H \omega_y^*}, \quad (27)$$

where

$$H = \{x > 0 \wedge y = 0 \wedge \omega_y^* \leq -4.5 + 0.04t^*\}. \quad (28)$$

From Eqs. (26)–(28), it is established that the center of the primary vortex core is the center of the vorticity distribution within the region H enclosed by a vorticity contour $\omega_y^* = -4.5 + 0.04t^*$. This establishment is to obtain the center of the vortex eye, where the vortex particles move around. The primary vortex ring is enlarged when it moves down toward the plane. However, it moves slightly upward at the position of $x/R \approx 1.8$ due to its interaction with the second vortex ring. In the final stage, the primary vortex ring moves slightly downward and is extended horizontally. The results of the present simulation agree well with the existing results.

The dynamics of a three-dimensional vortex structure, induced by the collision of a vortex ring with a plane, is shown in Fig. 6. When the primary vortex ring moves toward the plane, a disc-shaped boundary layer is formed on the plane, as shown at $t^* = 12$. This layer rolls up to form the secondary vortex ring at $t^* = 16$ and interacts with the primary vortex ring at $t^* = 18$. From $t^* = 20$, the secondary vortex ring decreases in size and moves slightly downward, whereas the primary ring continues increasing in size horizontally. The strength of both the vortex rings reduces with time due to the effect of vortex diffusion, as explained later.

The time evolution of the total kinetic energy and enstrophy are shown in Fig. 7, where $E_k(t)$ and $E_s(t)$ are calculated as

$$E_k(t) = \frac{1}{L_x L_y L_z} \iiint_{\Omega} 0.5 \mathbf{u}^2 dx dy dz, \quad (29)$$

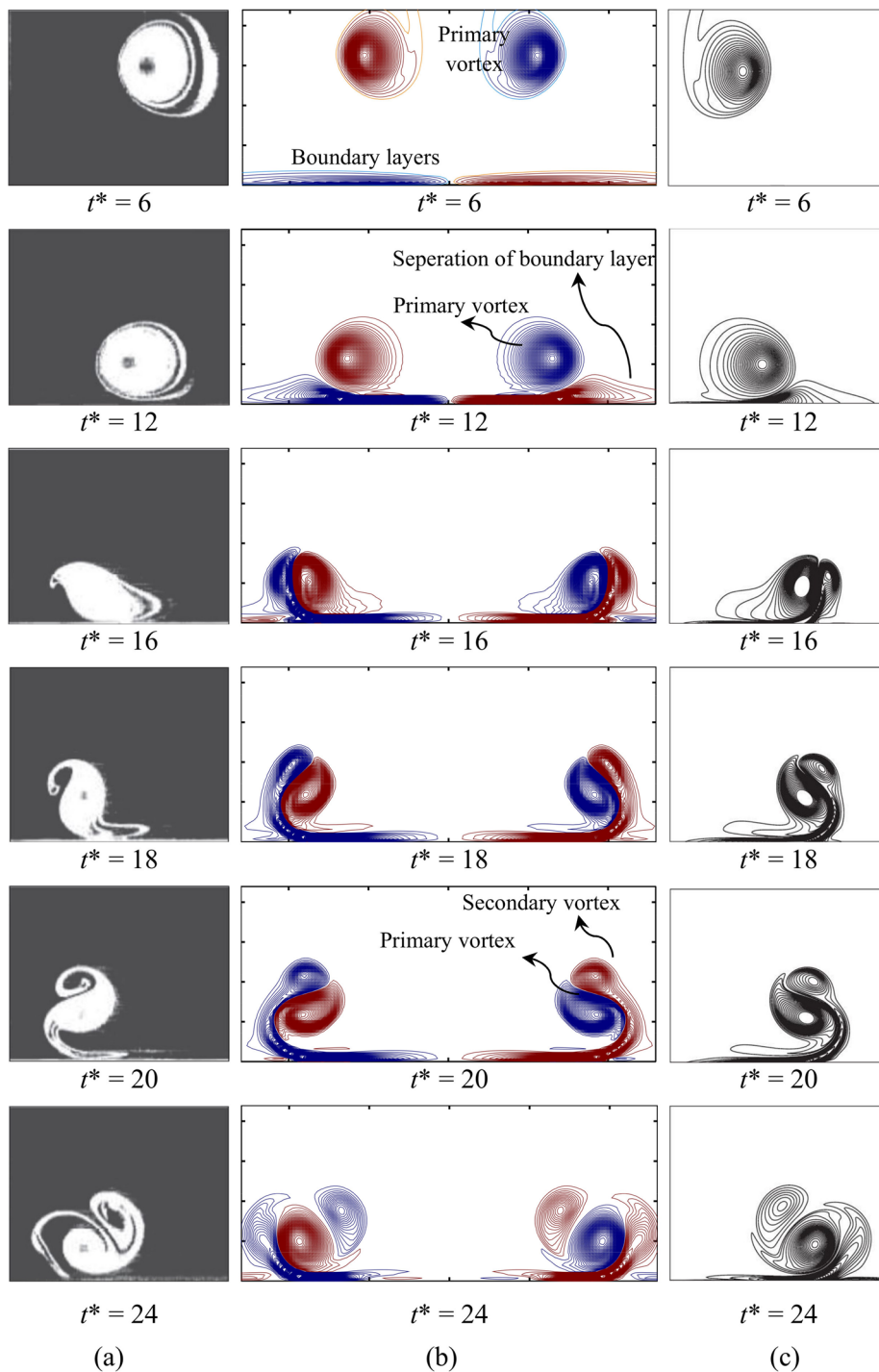


FIG. 4. Time evolution of collision of vortex ring with solid plane: results of experiment (a),⁹ present simulation (b), and Lattice Boltzmann (LBM) method (c).¹⁵ In (b), the positive and negative values of the vorticity component ω_z^* are represented in red and blue with the color scale in the range from -0.5 to 0.5 .

$$E_s(t) = \frac{1}{L_x L_y L_z} \iiint_{\Omega} 0.5 \omega^2 dx dy dz, \quad (30)$$

respectively, where L_x , L_y , and L_z are the sizes of the domain. There is a decrease in the total kinetic energy during the entire period of

evolution owing to its transformation into thermal energy. The enstrophy, which represents the total vorticity in the domain, reduces gradually from $t^* = 0$ to $t^* \approx 8$, as the effect of vortex diffusion is greater than those of the vortex stretching and penalization term. It is observed that the vortex diffusion creates a flow around

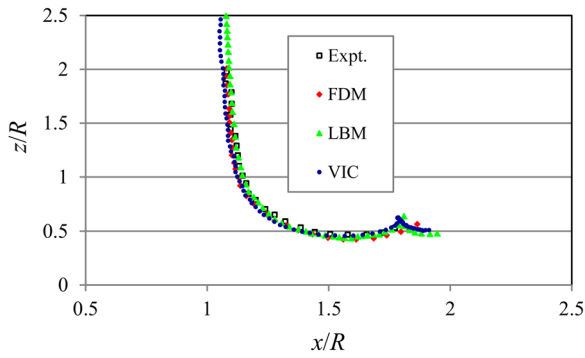


FIG. 5. Displacement of primary vortex core in the x - z plane: Plots are obtained by Expt. (black dotted line), FDM (red dotted line), LBM (green dotted line),⁹ and VIC (blue dotted line).¹⁵

the vortex ring with a reduction in the total vorticity. The stretching of the vortex is due to the transformation of the vortex structure from two dimensions, in which the vorticity is composed of ω_x and ω_y , to three dimensions, in which the vorticity is composed of ω_x ,

ω_y , and ω_z , and an increase in the total vorticity. The effect of the penalization term accounts for the generation of the vorticity induced by the body surface, as explained later. From $t^* = 8$ to $t^* = 15$, the enstrophy increases significantly when the boundary layer separates from the plane. During this period, the vorticity induced by the solid surface is higher than the effect of vortex diffusion. The enstrophy is maximum at $t^* = 15$ when the second vortex ring is formed. From $t^* = 16$, the enstrophy decreases because the generation of the vorticity induced by the interaction of the flow with the body surface is less than the vortex diffusion effects. The time evolution of the total kinetic energy and enstrophy are calculated at four grid resolutions, as shown in the legend and are found to be convergent with an increase in the grid nodes.

Figure 8 shows the effects of vortex stretching (Term I), vortex diffusion (Term II), and penalization (Term III) terms on the time evolution of the rate of change of enstrophy, based on the concept by Chu *et al.*,⁸ as formulated in detail in Appendix. From $t^* = 0$ to $t^* = 6$, the effects of these terms are low and the strength of the primary vortex ring remains almost unchanged as it is far from the plane. From $t^* = 6$ to $t^* \approx 15$, the effects of terms I and III on the rate of change of enstrophy increase significantly, whereas a considerable reduction is observed due to term II. The explanation for this is that when the primary vortex ring is near the plane, the boundary

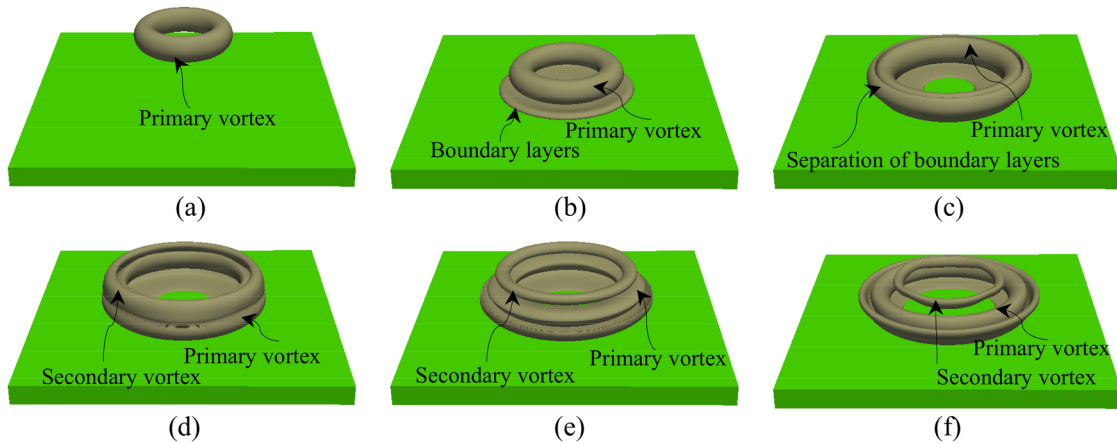


FIG. 6. Dynamics of vortex structure induced by collision of vortex ring with a plane. Isosurface of the vorticity magnitude plotted at $|\omega^*| = 1$. (a) $t^* = 6$. (b) $t^* = 12$. (c) $t^* = 16$. (d) $t^* = 18$. (e) $t^* = 20$. (f) $t^* = 24$.

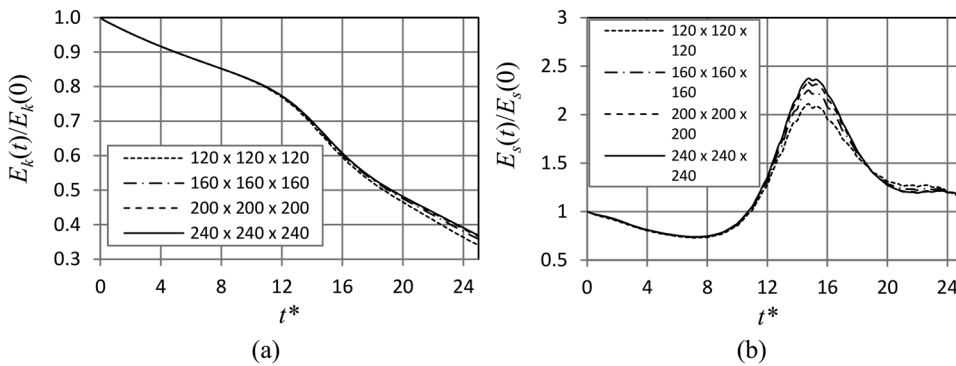


FIG. 7. Time evolution of total kinetic energy, $E_k(t)$, represented in (a) and total enstrophy, $E_s(t)$, represented in (b). The values of $E_k(t)$ and $E_s(t)$ are calculated in the whole computational domain at four grid resolutions shown in the legend.

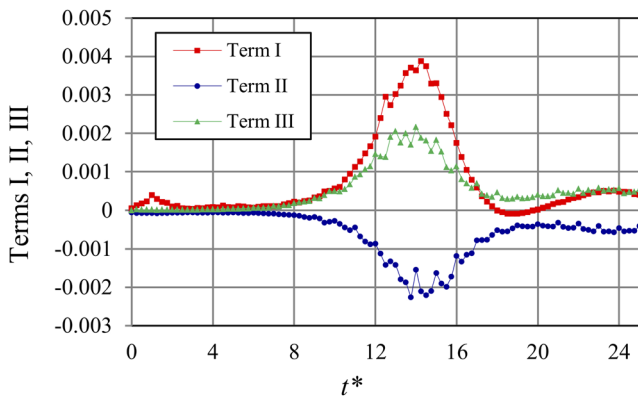


FIG. 8. Effects of vortex stretching (Term I), vortex diffusion (Term II), and penalization term (Term III) on the rate of change of enstrophy.

layer is formed which rolls up to form the secondary vortex ring causing an increase in the total vorticity. During this period, the interaction between the primary vortex ring and the body surface generates the vorticity (Term III) and is the cause of transformation of the vortex structure from two to three dimensions (Term I). When the vortex structure is transformed to three dimensions, the effect of the diffusion term increases simultaneously, due to the diffusion of three components of vorticity. The maximum effects of these terms are observed at $t^* \approx 15$, at which time the secondary vortex ring is completely formed. This is followed by a subsequent reduction in the rate of change of enstrophy. This is because the interaction of the primary vortex ring with the secondary ring plays a main role in the dynamics of the vortex structure. Once the secondary vortex ring is completely formed, the interaction between the primary vortex ring and the boundary layer becomes weak, leading to a decrease in the generation of vorticity from the solid body. From the figure, it can be seen that the effects of the vortex stretching and penalization terms always lead to an increase in the total vorticity, whereas a reduction is caused due to vortex diffusion.

B. Coaxial collision of a vortex ring with a sphere

The time evolution of deformation of a vortex ring caused by its impingement on a sphere is numerically investigated. The conditions for the simulation, similar to those in the experiment, are shown in Fig. 9. The diameter of the sphere is $D = 30$ mm. A piston moves from B to A at a speed of $u_{piston(B \rightarrow A)} = 3.33$ mm/s and then from A to B at $u_{piston(A \rightarrow B)} = 5$ mm/s. A computational domain of $2.33D \times 2.33D \times 4.66D$ is discretized into $200 \times 200 \times 400$ cube cells and the nondimensional time step, $\Delta t^* = \Delta t u_{piston(A \rightarrow B)} / D$, is 1.667×10^{-4} . The nondimensional time, component of vorticity, and magnitude of vorticity are defined as $t^* = t u_{piston(A \rightarrow B)} / D$, $\omega_y^* = \omega_y (D / u_{piston(A \rightarrow B)})$, and $|\omega^*| = |\omega| (D / u_{piston(A \rightarrow B)})$, respectively. The kinematic viscosity of the fluid is $\nu = 1$ mm²/s. In this case, the solid velocity of Eq. (14) is given by

$$\mathbf{u}_s^1 = \mathbf{u}_{sphere} = 0, \tag{31}$$

$$\mathbf{u}_s^2 = \mathbf{u}_{cylinder} = 0, \tag{32}$$

$$\mathbf{u}_s^3 = \mathbf{u}_{piston}. \tag{33}$$

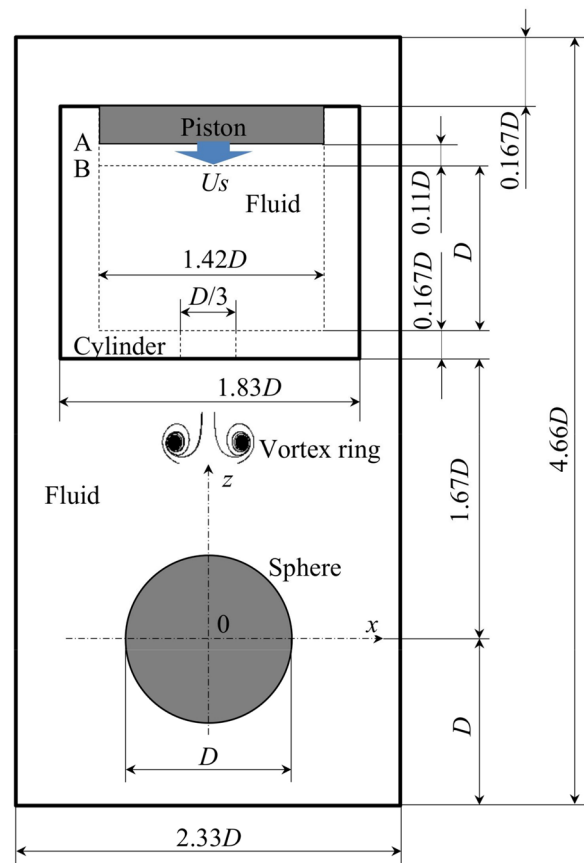


FIG. 9. Configuration of simulation conditions of the coaxial collision of a vortex ring with a sphere.

Figure 10 shows the early stage of formation of the vortex rings. At $t^* = 0.083$ and 0.167 , the piston moves upward and a vortex ring is formed inside the cylinder due to rolling up of the shear layer generated at the tip of the cylinder. At $t^* = 0.25$, the piston moves downward and a primary vortex ring starts forming outside the cylinder whereas the ring inside the cylinder continues moving upward. At $t = 0.333$, the vortex ring inside the cylinder collides with the piston, while the primary vortex ring outside the cylinder is completely formed. In this study, the characteristics of the collision of the primary vortex ring with a sphere are investigated, whereas a discussion of the collision of the vortex ring with the piston inside the cylinder is omitted.

The characteristics of the primary vortex ring at $t^* = 0.333$ are examined. The estimated diameter of the primary vortex ring is $D_{pv} = 0.444D$, shown in Fig. 13. The circulation of the vortex at this time is calculated by taking the integrals of the vorticity distribution ω_y over regions in the x - z plane passing through the center of the vortex-ring as follows:^{29,27}

$$\Gamma_{(t^*=0.333)} = \frac{1}{2} \iint_{A^+} \omega_y dx dz - \frac{1}{2} \iint_{A^-} \omega_y dx dz = \iint_{A^+} \omega_y dx dz. \tag{34}$$

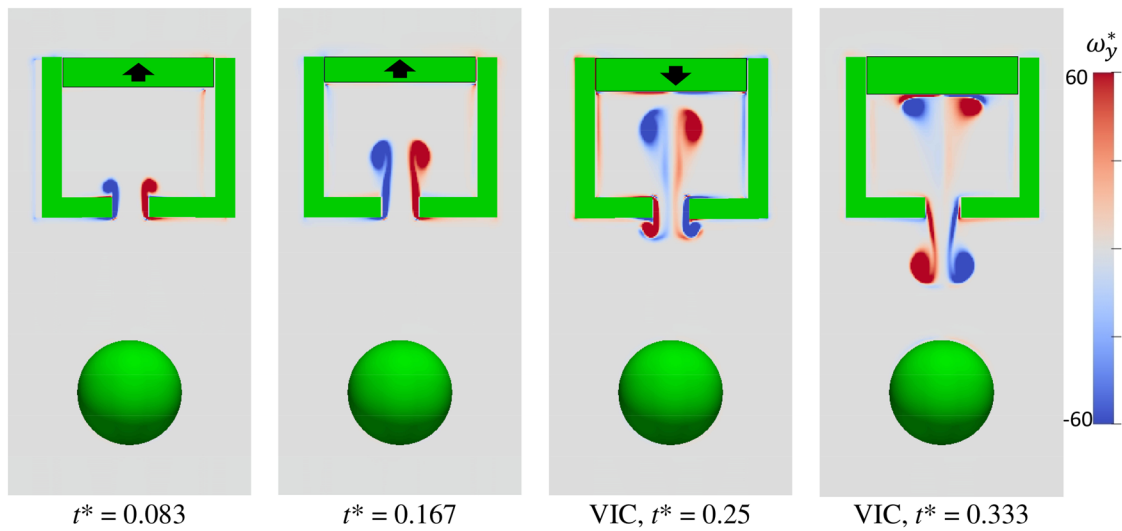


FIG. 10. Formation of primary vortex ring.

The regions A^+ and A^- are shown in Fig. 11. The circulation is calculated in these regions to avoid the effect of a vortex at the cylinder tip, while still considering the effect of the wake of the primary vortex ring, and its value is $\Gamma = 1030 \text{ mm}^2/\text{s}$. The radius of the core of the primary vortex ring is estimated using the formula of Swearingen *et al.*,¹⁰ as follows:

$$\sigma = \sqrt{\frac{\iint_{B^+} \rho^2(x, z) \omega_y dx dz}{\iint_{B^+} \omega_y dx dz}}, \quad (35)$$

where $\rho^2(x, z) = (x - x_c)^2 + (z - z_c)^2$ and $(x_c, z_c) = (-0.222D, 1.173D)$, obtained using Eqs. (26) and (27), are the coordinates of the center of the vorticity distribution within the region B^+ . Region B^+ belongs to region A^+ and is enclosed by a vorticity contour of $\omega_y^* = 132$, as shown in Fig. 11. The estimated radius of the vortex core is $\sigma_{simulation} = 0.055D$. The radius of the vortex core can also be obtained using the experimental Saffman formula³⁰

$$\sigma = \sqrt{4\nu T}, \quad (36)$$

where $T = 0.66 \text{ s}$ is the stroke time of the piston moving from A to B. The radius of the core estimated using formula (36) is $\sigma_{experiment} = 0.054D$ and the relative error between the simulation and experimental measurement is 1.85%. The calculated Reynolds number of the vortex ring, Re_Γ , is 1030.

Figure 12 shows the dynamics of the two-dimensional vortex structure induced by the coaxial collision of a vortex ring with a sphere. When the primary vortex ring moves toward the sphere, a boundary layer is formed at $t^* = 0.333$ and 0.418 as shown in the figure. This boundary layer separates from the surface of the sphere at $t^* = 0.5$ due to the effect of the primary vortex ring and rolls up to form the secondary vortex ring at $t^* = 0.583$, as shown in a three-dimensional figure later. From $t^* = 0.667$, the secondary vortex ring interacts with the primary ring in which the motion of the secondary ring around the primary ring is observed to be the same as that in the case of collision of a vortex ring with a plane. The boundary layer continues to separate from the surface of the sphere and encloses the primary vortex ring. In the experiment, the ink is only injected from the cylinder, and therefore, the formations of the boundary layer and the secondary vortex ring are not observed completely. In general, the results of the dynamics of the vortex

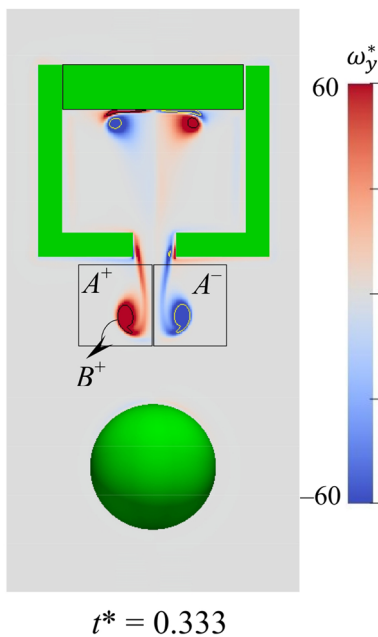


FIG. 11. Configuration of the areas A^+ , A^- , and B^+ used to calculate the circulation, vortex core center, and radius.

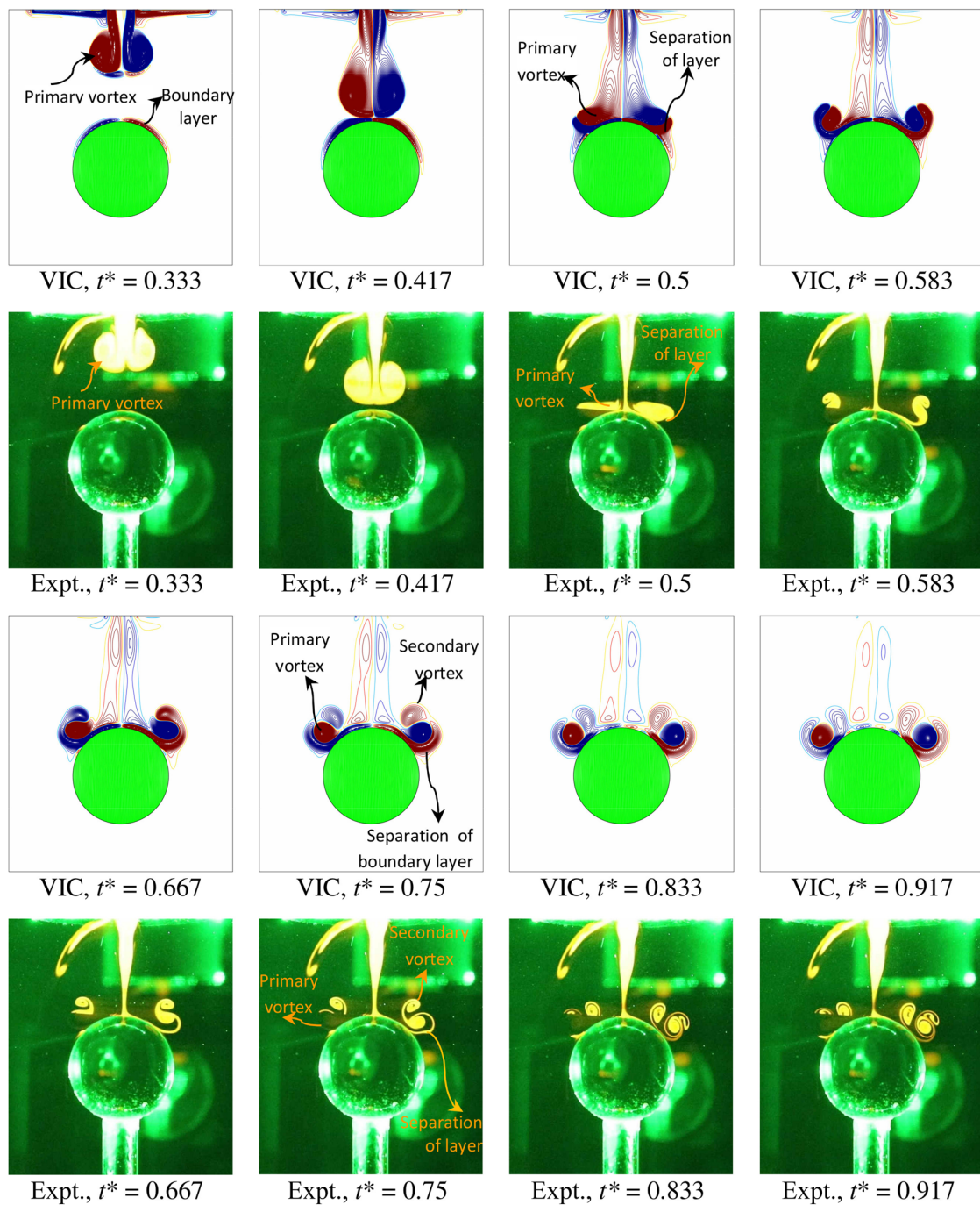


FIG. 12. Time evolution of two-dimensional vortex structure induced by coaxial collision of vortex ring with sphere on the x - z plane. The simulation and experimental results are visualized by the vorticity component ω_y and ink, respectively. The positive and negative values of the vorticity component ω_y are shown in red and blue, respectively.

structure obtained by the simulation agree with the experimental results.

Figures 13 and 14 show the time evolution of the diameter and vertical displacement, and the displacement on the x - z plane

of the vortex cores, respectively. As the primary vortex ring moves toward the sphere, its diameter increases sharply at first from $t^* = 0$ to $t^* = 0.5$, then gradually on coming in contact with the sphere, as seen in Fig. 13(a). The secondary vortex ring, which is formed

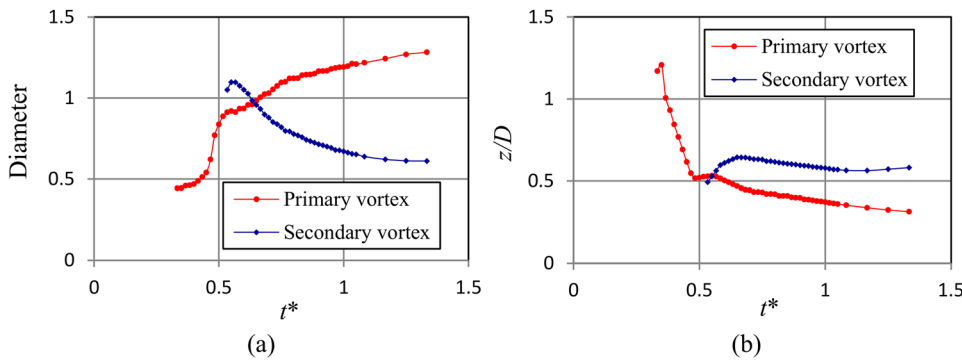


FIG. 13. Time evolution of diameter and vertical (z-direction) displacement of vortex cores represented in figures (a) and (b), respectively.

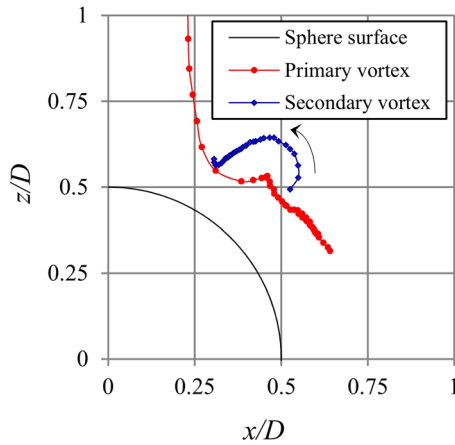


FIG. 14. Displacement of vortex cores on x-z plane.

from $t^* = 0.5$, enlarges slightly in a short time and subsequently reduces in size gradually. The secondary vortex ring moves around toward the center of the primary vortex ring. This is explained as a fact that the strength of the primary vortex ring is greater than

that of the secondary vortex ring, resulting in a nonzero value of the total circulation of vortex pair, leading to a net rotation of the vortex system. This system rotates around a nonstationary point laying on an orbit which is most influenced by the primary vortex ring. Additional explanations of the interaction of the vortex pair are found in investigations by Meunier *et al.*³¹ and Forster *et al.*³² In addition, when the secondary vortex ring is formed, its location is always higher than that of the primary ring, as shown in Fig. 13(b). The primary vortex ring appears to slip on the surface of the sphere, whereas the secondary ring is pushed up and dwindles in size, as shown in Fig. 14. The diameter and displacement of the vortices are calculated using the position of the centers of vortex eyes obtained by choosing the pixels of the high resolution images corresponding to the centers of the vorticity contours with the smallest shapes.

The time evolution of the three-dimensional vortex structure induced by the coaxial collision of a vortex ring with a sphere is shown in Fig. 15. The boundary layer is formed when the primary vortex ring is near the surface of the sphere at $t^* = 0.417$. Subsequently, the secondary vortex ring is formed due to the interaction of the primary vortex ring with the boundary layer, as shown at $t^* = 0.5$ and 0.585 . The strength of the vortex rings decreases with time owing to their mutual interaction, at $t^* = 0.667$. At $t^* = 0.75$, the secondary vortex ring disappears, although it is displayed on the

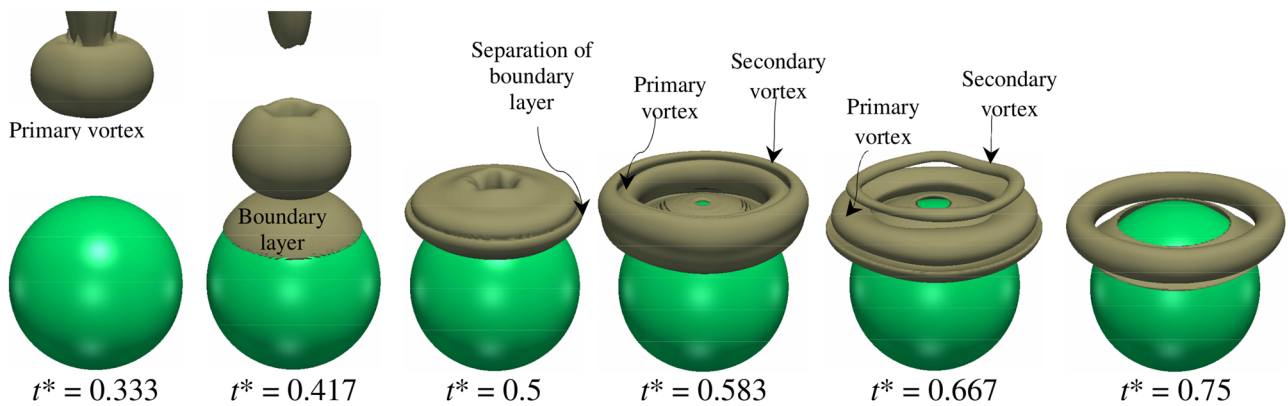


FIG. 15. Time evolution of three-dimensional vortex structure induced by coaxial collision of vortex ring with sphere. Isosurface of magnitude of vorticity is plotted at $|\omega^*| = 18$.

x - z plane in Fig. 12. This is because the magnitude of the vorticity at $|\omega^*| = 18$ is higher than that of the maximum vorticity of the second vortex ring. The vorticity component ω_z is very small compared with the components ω_x and ω_y . The dynamics of the vortex structure almost remain in two dimensions.

C. Noncoaxial collision of a vortex ring with a sphere

The simulation and experimental conditions in the noncoaxial collision of a vortex ring with a sphere are the same as in the coaxial collision, except that the vertical centerlines of the sphere

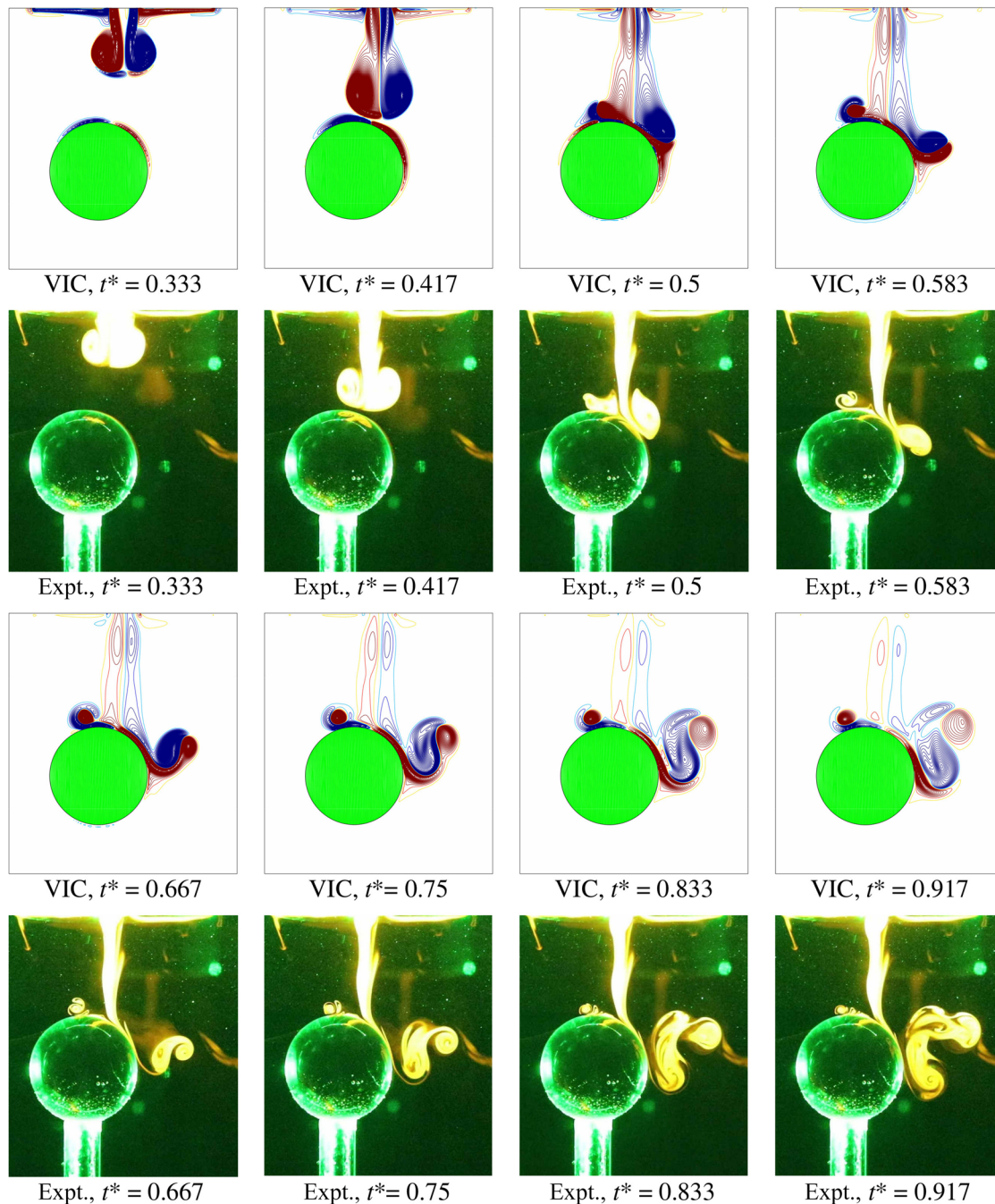


FIG. 16. Time evolution of vortex structure induced by noncoaxial collision of vortex ring with sphere on the x - z plane. The simulation and experimental results are visualized by the vorticity component ω_y and ink, respectively. The positive and negative values of the vorticity component ω_y are shown in red and blue, respectively.

and cylinder differ by $L = D/4$, i.e., the distance between the vertical centerlines of the sphere and primary vortex ring at $t^* = 0.333$ is $L = D/4$.

Figure 16 shows the time evolution of the two-dimensional vortex structure induced by the noncoaxial collision of a vortex ring with a sphere. A boundary layer is formed when the primary vortex ring moves toward the sphere, at $t^* = 0.333$ as shown in the figure; however, there is a phase difference between the centerline of the layer and vertical centerline of the sphere. At $t^* = 0.417$, the thickness of the layer increases significantly when the primary vortex ring is close to the sphere. The primary vortex ring interacts with the boundary layer at $t^* = 0.5$, leading to a separation of the boundary layer at $t^* = 0.583$. On the left of the sphere, a weak interaction between the primary vortex ring (represented in red) and the boundary layer (represented in blue) is similar to that in the coaxial collision, as shown at $t^* \geq 0.667$. However, the location of the vortex core does not appear to change with time. On the right of the sphere, the primary vortex core (represented in blue) rotates around its center and pushes the boundary layer (represented in red) far away from the sphere at $t^* = 0.667$. At this time, the boundary layer rolls up to form the secondary vortex and continues to separate from the surface of the sphere. Subsequently, the primary vortex core interacts with the secondary vortex as well as the separated boundary layer at $t^* = 0.75$ as a result of which the primary vortex core splits into two, as shown at $t^* = 0.833$ and 0.917 . The results obtained by the simulation and the experiment agree with each other.

Figure 17 shows the time evolution of the vorticity component ω_x on the three vertical planes $x/D = 0$, $x/D = 0.25$, and $x/D = 0.5$. The

planes $x/D = 0$ and $x/D = 0.25$ pass through the vertical centerlines of the sphere and cylinder, respectively, whereas the plane $x/D = 0.5$ is a vertical tangential plane of the sphere. The characteristics of the interaction between the primary vortex core and boundary layer on the planes $x/D = 0$ and $x/D = 0.25$ are similar to those in the coaxial collision. However, the interaction on the plane $x/D = 0$ is so weak that the secondary vortex core is not observed in the noncoaxial collision. In addition, at $t^* = 0.583$, the angle of rotation of the primary vortex core around its center on the plane $x/D = 0$ is more than that on the plane $x/D = 0.25$. On the plane $x/D = 0.5$, the primary vortex core appears to slip on the boundary layer at $t^* = 0.583$, breaking it and leading to the formation of the secondary vortex core at $t^* = 0.667$.

Figure 18 describes the time evolution of the three-dimensional vortex structure induced by the noncoaxial collision of a vortex ring with a sphere. The plots in the upper and lower rows of the figure are the isosurface of the magnitude of the vorticity $|\omega|$ and vorticity component ω_z , respectively. The upper row depicts the deformation of the primary vortex ring when it collides with the sphere. The circulation is unequal at the cross sections of the primary vortex ring; the secondary vortex is not a ring and interacts strongly with half of the primary vortex ring on the right of the sphere. The lower row shows a significant development in the vorticity component ω_z when the primary vortex ring reaches the sphere. This is completely different from the case of coaxial collision in which the values of this component are negligible. The structure of the vorticity component ω_z is similar to the structure of the magnitude of the vorticity ω .

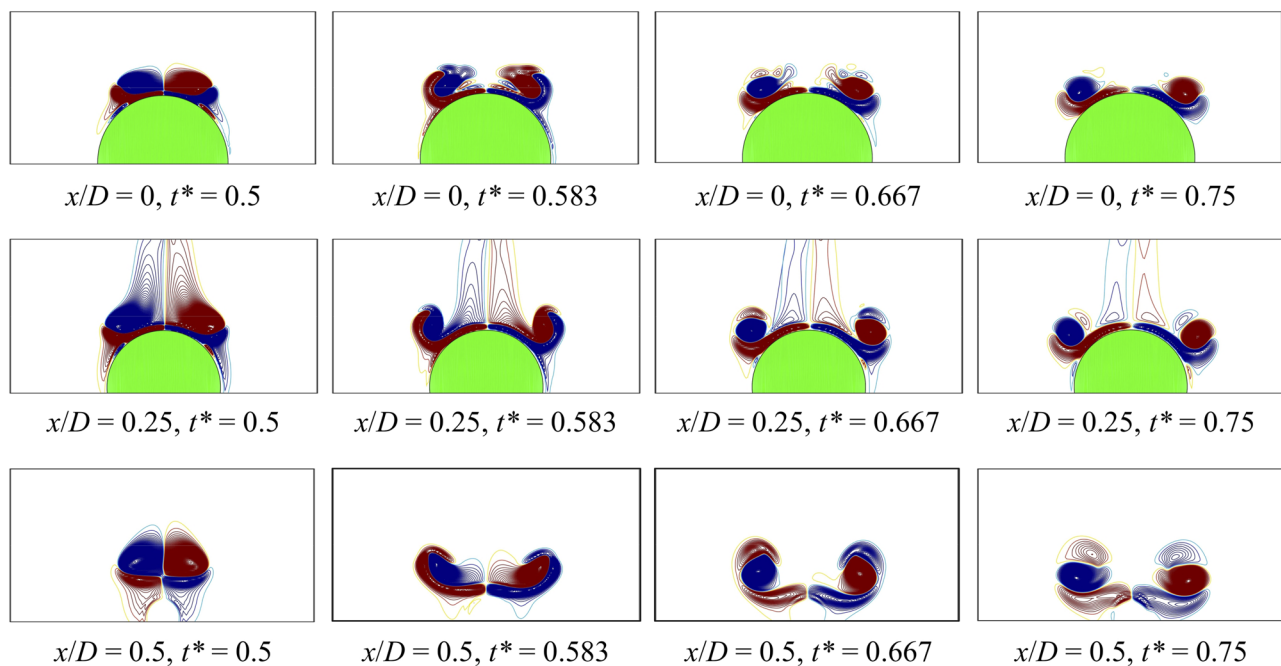


FIG. 17. Time evolution of two-dimensional vortex structure induced by noncoaxial collision of vortex ring with sphere at three cross sections. The simulation results are visualized by the vorticity component ω_x on three planes, $x/D = 0$, $x/D = 0.25$, and $x/D = 0.5$, as plotted in the rows 1, 2, and 3, respectively.

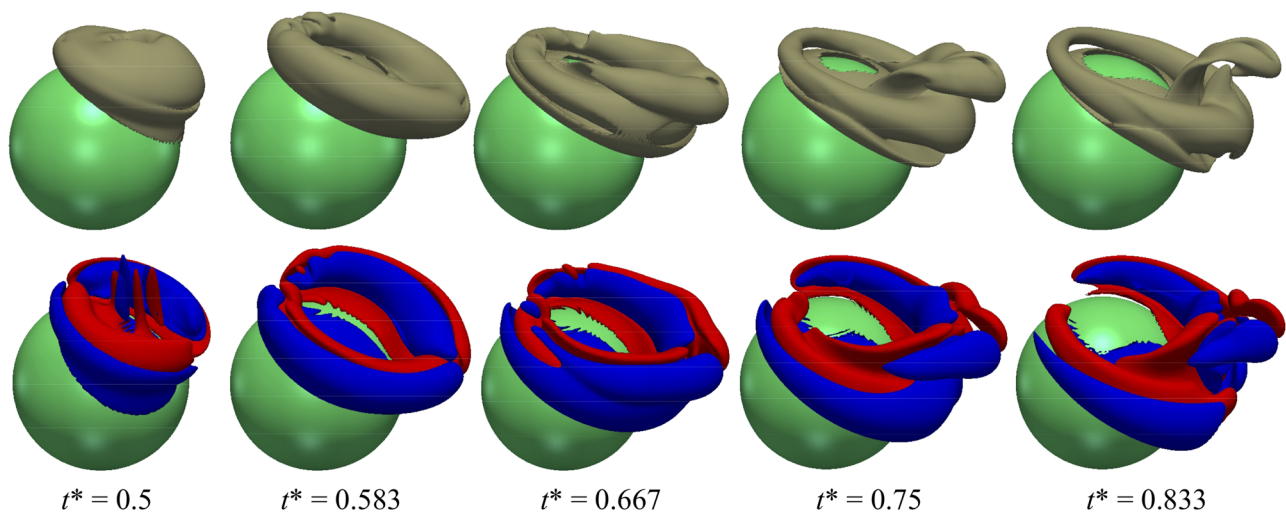


FIG. 18. Time evolution of three-dimensional vortex structure induced by noncoaxial collision of vortex ring with sphere. In the upper row, the isosurface of the magnitude of the vorticity is plotted at $|\omega^*| = 18$. In the lower row, the vorticity component is plotted at $\omega_z^* = \pm 6$ represented in red and blue, respectively, where $\omega_z^* = \omega_z(D/u_{piston(A \rightarrow B)})$.

Figure 19 shows the time evolution of the total kinetic energy and enstrophy of the coaxial and noncoaxial collisions of a vortex ring with a sphere. In general, the curves are similar to those in the collision of a vortex ring with a solid plane. A gradual decrease in the kinetic energy during the entire period is observed in the coaxial as well as noncoaxial collisions and the behavior in both the cases is similar. The total enstrophy reduces slightly from $t^* = 0$ to $t^* \approx 0.416$, before a sharp increase from $t^* \approx 0.416$ until $t^* \approx 0.5$ at which time the secondary vortex ring is completely formed, after which it continues to decrease. In particular, the maximum total enstrophy in the coaxial collision is higher than that in the noncoaxial collision. This is because the effect of vortex diffusion in the noncoaxial collision is greater than that in the coaxial collision. The vortex structure in the noncoaxial collision is in three dimensions, leading to the

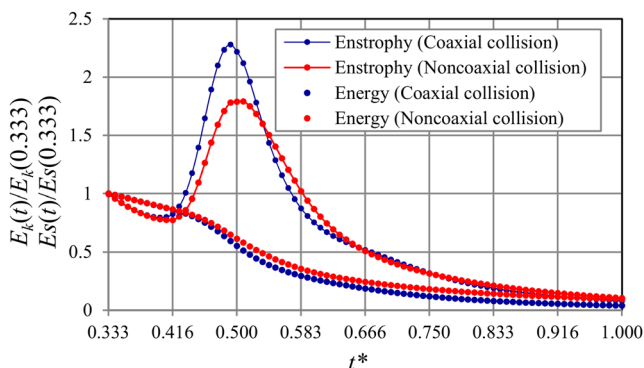


FIG. 19. Time evolution of total kinetic energy and enstrophy of coaxial and noncoaxial collisions of vortex ring with sphere: The values are calculated in the computational domain $(-1.165D, 1.156D) \times (-1.165D, 1.156D) \times (-D, 1.65D)$ to avoid the effects of the vortex ring inside the cylinder and the shear layers at the cylinder tip.

diffusion of three components of the vorticity, whereas that in the coaxial collision is in two dimensions, corresponding to the diffusion of two components, ω_x and ω_y . The effects of the vortex stretching, a cause of the production of vorticity component ω_z , in the noncoaxial collision are greater than those in the coaxial collision. However, the difference in the effects of the penalization term in the two is negligible.

IV. CONCLUSIONS

A VIC method was developed to simulate the deformation of a vortex ring caused by its impingement on a rigid surface. The numerical method was first validated by simulating the collision of a vortex ring with a rigid planar surface. The displacement of the primary vortex core and the distribution of the vorticity in two dimensions agree well with the existing results. We carried out the investigation of coaxial and noncoaxial collisions of a vortex ring with a spherical surface by an experiment as well as by simulation. The results of the dynamics of the vortex structure obtained by simulation agree well with the experimental results. The highlights of the study are given below:

- (1) In the coaxial collision, the secondary vortex ring is formed when the primary vortex ring moves toward the sphere and there is a mutual interaction between them. The secondary vortex ring moves around the primary ring and its size reduces gradually whereas the size of the primary ring increases and it moves slightly downward. The vortex structure almost remains in two dimensions, in which the vorticity comprises two components, ω_x and ω_y .
- (2) In the noncoaxial collision, the secondary vortex that is observed is not a vortex ring, although at some cross sections of the side view, the behavior of the vortex dynamics is similar to that in the coaxial collision. The circulation of the primary vortex ring is unequal at all the cross sections. In addition,

the vortex structure is three-dimensional, and there is a significant development of the vorticity component ω_z when the primary vortex ring reaches the sphere.

- (3) The total kinetic energy in the two cases reduces gradually over the entire time evolution due to its transformation into thermal energy. The enstrophy reduces gradually in the early stage due to the effect of vortex diffusion and increases considerably when the primary vortex ring reaches the sphere. The enstrophy reaches a maximum value when the secondary vortex is completely formed before decreasing gradually. This is because the effects of the vortex stretching and penalization terms are lower than that of vortex diffusion. The interaction between the primary and secondary vortices plays a main role in this period. In this study, only a single Reynolds number and the fixed diameter of the sphere are used to investigate the vortex dynamics. The effects of these parameters on the flow phenomena are of interest in future investigations.

ACKNOWLEDGMENTS

This study was supported by a grant from the Project of Creation of Life Innovation Materials for Interdisciplinary and International Researcher Development of the Ministry of Education, Culture, Sports, Science and Technology, Japan.

APPENDIX: RATE OF CHANGE OF ENSTROPY

The total enstrophy of the flow is rewritten as

$$E_s(t) = \frac{1}{L_x L_y L_z} \iiint_{\Omega} 0.5 \omega^2 dx dy dz. \tag{A1}$$

The rate of change of enstrophy is expressed as

$$\begin{aligned} \frac{D(E_s(t))}{Dt} &= \frac{1}{L_x L_y L_z} \iiint_{\Omega} \frac{D(0.5 \omega^2)}{Dt} dx dy dz \\ &= \frac{1}{L_x L_y L_z} \iiint_{\Omega} \frac{\omega D\omega}{Dt} dx dy dz. \end{aligned} \tag{A2}$$

Substituting the following momentum equation

$$\frac{D\mathbf{\omega}}{Dt} = \frac{\partial \mathbf{\omega}}{\partial t} + (\mathbf{u} \cdot \nabla) \mathbf{\omega} = (\mathbf{\omega} \cdot \nabla) \mathbf{u} + \nu \nabla^2 \mathbf{\omega} + \nabla \times [\lambda \chi_s (\mathbf{u}_s - \mathbf{u})] \tag{A3}$$

into Eq. (A2), the result is obtained as

$$\begin{aligned} \frac{D(E_s(t))}{Dt} &= \frac{1}{L_x L_y L_z} \iiint_{\Omega} \underbrace{\omega \cdot [(\mathbf{\omega} \cdot \nabla) \mathbf{u}]}_{\text{Term I = stretching effects}} dx dy dz \\ &+ \frac{1}{L_x L_y L_z} \iiint_{\Omega} \underbrace{\omega \cdot (\nu \nabla^2 \mathbf{\omega})}_{\text{Term II = diffusion effects}} dx dy dz \\ &+ \frac{1}{L_x L_y L_z} \iiint_{\Omega} \underbrace{\omega \cdot [\nabla \times (\lambda \chi_s (\mathbf{u}_s - \mathbf{u}))]}_{\text{Term III = penalization effects}} dx dy dz. \end{aligned} \tag{A4}$$

The first, second, and third terms on the right-hand side of Eq. (A4) express the effects of stretching, diffusion, and penalization, respectively, on the rate of change of enstrophy.

REFERENCES

- ¹M. Cheng, J. Lou, and T. T. Lim, "Leapfrogging of multiple coaxial viscous vortex rings," *Phys. Fluids* **27**(3), 031702 (2015).
- ²M. Cheng, J. Lou, and T. T. Lim, "Evolution of an elliptic vortex ring in a viscous fluid," *Phys. Fluids* **28**(3), 037104 (2016).
- ³T. Hiejima, "Streamwise vortex breakdown in supersonic flows," *Phys. Fluids* **29**(5), 054102 (2017).
- ⁴D. Zhang, L. Cheng, H. An, and M. Zhao, "Direct numerical simulation of flow around a surface-mounted finite square cylinder at low Reynolds numbers," *Phys. Fluids* **29**(4), 045101 (2017).
- ⁵J. D. A. Walker, C. R. Smith, A. W. Cerra, and T. L. Doligalski, "The impact of a vortex ring on a wall," *J. Fluid Mech.* **181**, 99–140 (1987).
- ⁶T. T. Lim, T. B. Nickels, and M. S. Chong, "A note on the cause of rebound in the head-on collision of a vortex ring with a wall," *Exp. Fluids* **12**(1-2), 41–48 (1991).
- ⁷C. H. Liu, "A three-dimensional vortex particle-in-cell method for vortex motions in the vicinity of a wall," *Numer. Methods Fluids* **37**(5), 501–523 (2001).
- ⁸C. C. Chu, C. T. Wang, and C. S. Hsiehb, "An experimental investigation of vortex motions near surfaces," *Phys. Fluids* **5**(3), 662–676 (1993).
- ⁹C. C. Chu, C. T. Wang, and C. C. Chang, "A vortex ring impinging on a solid plane surface-vortex structure and surface force," *Phys. Fluids* **7**(6), 1391–1401 (1995).
- ¹⁰J. D. Swearingen, J. D. Crouch, and R. A. Handler, "Dynamics and stability of a vortex ring impacting a solid boundary," *J. Fluid Mech.* **297**, 1–28 (1995).
- ¹¹D. Fabris and D. Liepmann, "Quantitative experimental and numerical investigation of a vortex ring impinging on a wall," *J. Comput. Phys.* **8**(10), 2640–2649 (1996).
- ¹²M. Cheng, J. Lou, and L.-S. Luo, "Numerical study of a vortex ring impacting a flat wall," *J. Fluid Mech.* **660**, 430–455 (2010).
- ¹³T. H. New, B. Zang, B. Zang, S. Shi, and S. Long, "Impact of vortex-rings upon V-shaped walls," in *19th International Symposium on the Application of Laser and Imaging Techniques to Fluid Mechanics, Portugal* (Instituto Superior Técnico, 2018), p. 11.
- ¹⁴Q. Li and C. H. Bruecker, "Vortex interaction with a rough wall formed by a hexagonal lattice of posts," *Phys. Fluids* **30**(5), 054107 (2018).
- ¹⁵M. Cheng, J. Lou, and T. T. Lim, "A numerical study of a vortex ring impacting a permeable wall," *Phys. Fluids* **26**(10), 103602 (2014).
- ¹⁶P. Poncet, "Méthodes particulières pour la simulation des sillages tridimensionnels," Ph.D. thesis, University Joseph Fourier, Grenoble, France, 2001.
- ¹⁷J. J. Allen, Y. Jouanne, and B. N. Shashikanth, "Vortex interaction with a moving sphere," *J. Fluid Mech.* **587**, 337–346 (2007).
- ¹⁸B. U. Felderhofs, "Coaxial collisions of a vortex ring and a sphere in an inviscid incompressible fluid," *Phys. Fluids* **29**(4), 043601 (2017).
- ¹⁹G.-H. Cottet and P. Poncet, "Advances in direct numerical simulations of 3D wall-bounded flows by vortex-in-cell methods," *J. Comput. Phys.* **193**(1), 136–158 (2003).
- ²⁰L. A. Barba, A. Leonard, and C. B. Allen, "Numerical investigations of the accuracy of the vortex method with and without remeshing," in *16th AIAA Computational Fluid Dynamics Conference, Florida* (AIAA, 2003), p. 11.
- ²¹T. Uchiyama, Y. Yoshii, and H. Hamada, "Direct numerical simulation of a turbulent channel flow by an improved vortex in cell method," *Int. J. Numer. Methods Heat Fluid Flow* **24**(1), 103–123 (2014).
- ²²J. P. Christiansen, "Numerical simulation of hydrodynamics by the method of point vortices," *J. Comput. Phys.* **13**(3), 363–379 (1973).
- ²³G.-H. Cottet and P. D. Koumoutsakos, *Vortex Methods: Theory and Practice* (Cambridge University Press, 2000).
- ²⁴V. L. Nguyen, R. Z. Lavi, and T. Uchiyama, "Numerical simulation of flow around two tandem cylinders by vortex in cell method combined

with immersed boundary method,” *Adv. Appl. Fluid Mech.* **19**(4), 787–810 (2016).

²⁵T. Uchiyama and Y. Yoshii, “Numerical study of the entrainment and transport of gas bubbles by a vortex ring,” *J. Chem. Eng. Process Technol.* **6**(4), 1000245–1000253 (2015).

²⁶V. L. Nguyen, T. Degawa, and T. Uchiyama, “Numerical simulation of annular bubble plume by vortex in cell method,” *Int. J. Numer. Methods Heat Fluid Flow* **29**(3), 1103–1131 (2019).

²⁷V. L. Nguyen, T. Degawa, and T. Uchiyama, “Numerical simulation of the interaction between a vortex ring and a bubble plume,” *Int. J. Numer. Methods Heat Fluid Flow* **29**(9), 3192–3224 (2019).

²⁸V. L. Nguyen, T. Degawa, T. Uchiyama, and K. Takamura, “Numerical simulation of bubbly flow around a cylinder by semi-Lagrangian–Lagrangian method,” *Int. J. Numerical Methods for Heat and Fluid Flow* (published online).

²⁹M. Bergdorf, P. Koumoutsakos, and A. Leonard, “Direct numerical simulations of vortex rings at $Re = 7500$,” *J. Fluid Mech.* **581**, 495–505 (2007).

³⁰I. S. Sullivan, J. J. Niemela, R. E. Hershberger, D. Bolster, and R. J. Donnelly, “Dynamics of thin vortex rings,” *J. Fluid Mech.* **609**, 319–347 (2008).

³¹P. Meunier, U. Ehrenstein, T. Leweke, and M. Rossi, “A merging criterion for two-dimensional co-rotating vortices,” *Phys. Fluids* **14**(8), 2757–2766 (2002).

³²K. J. Forster, T. J. Barber, S. Diasinos, and G. Doig, “Interactions of a co-rotating vortex pair at multiple offsets,” *Phys. Fluids* **29**(5), 057102 (2017).